

Ocean wind fields from satellite active microwave sensors

S. Zecchetto

Istituto Scienze dell'Atmosfera e del Clima

Padova, Italy

s.zecchetto@isac.cnr.it

1. The Marine Atmospheric Boundary Layer

"In the Earth's atmosphere, the planetary boundary layer is the air layer near the ground affected by diurnal heat, moisture or momentum transfer to or from the surface". This definition, obtained from ¹, may introduce the Marine Atmospheric Boundary Layer (MABL) as the planetary boundary layer over the sea surface. In this layer, important exchanges of sensible and latent heat and momentum take place over a large spectrum of time and spatial scales, driving the sea waves, the drift ocean currents and the storage of CO₂ by the sea due to the wind and the breaking waves. In this context, the leading quantity is the wind vector \mathbf{U} . Its assessment is of paramount importance in the evaluation of the wind stress $\tau = C_d(T_a, T_s, T_d) \cdot |\mathbf{U}|^2$, (the drag coefficient C_d is a function depending, in a first approximation, on the air T_a , the sea T_s and the dew T_d temperatures), and of the gas transfer velocity $k = 2.8310^{-2} \cdot |\mathbf{U}|^3$ (Monahan, 2002), for instance.

One of the major problems in understanding the dynamics of the wind in the surface layer, the bottom layer inside the MABL where the turbulent fluxes exhibit a variability smaller than 10%, is the difficulty to get experimental data at spatial scales from few meters to few kilometers.

The satellite sensors discussed in this chapter measure the backscatter from the sea surface, providing maps directly related to the characteristics of the surface layer and to the wind blowing inside this layer. Satellite active microwave sensors are the only instruments able to provide information about the spatial structure of the wind in the marine surface layer over large areas.

2. Satellite active microwave sensors

The active microwave sensors (Campbell, 2002; CCRS, 2009; Elachi, 1988) are radars operating in the microwave region (1 to 30 GHz in frequency, 1 to 30 cm in wavelength) at different polarizations and incidence angles. Over the sea, the radar return depends, besides the geometry of the radar illumination, from the degree of development of the sea surface roughness (Valenzuela, 1978), composed by centimeter sea waves produced by the wind. Since the wind field has its own spatial pattern, which depends on its strength, on the thermodynamic characteristics at the air-sea interface and on the interaction between the wind

¹ http://en.wikipedia.org/wiki/Boundary_layer

flow and the orography, the sea surface roughness it generates its spatial features. The radar backscatter does reproduce, in turns, the sea surface roughness. Therefore, the study of the characteristics of the radar backscatter provides information on the characteristics of the wind and of the MABL.

The sea surface roughness is also modulated by some pre-existing oceanographic phenomena, like sea surface gravity waves, internal waves and ocean currents, or by the presence of oil slicks on the sea surface, which muffle the roughness. These modulations permit the detection of these oceanographic phenomena, besides the wind field.

This section introduces the two most popular radar sensors: the scatterometer, used to measure the wind field over the ocean, and the Synthetic Aperture Radar (SAR), used for a variety of applications, from land (forestry, geology, agriculture) to ocean (ocean surface waves, currents, ocean wind).

2.1 Spaceborne scatterometers

At present, the two most important satellites carrying scatterometers are the NASA *QuikSCAT* (JPL, 2006) and the Eumetsat *Metop* (Eumetsat, 2007). Both fly on a polar sun-synchronous orbit of about 100 minute of period. *QuikSCAT* has a repetition cycle of 4 days, whereas *Metop* of 29 days. This means that every 4 (29) days the scatterometers cover exactly the same areas of the Earth. The scatterometer winds are referenced to 10 m of height above the sea surface and to equivalent neutral air-sea stability conditions.

Scatterometer data are widely used by the scientific meteorologic community: they are assimilated into the global atmospheric models (Isaksen & Janssen, 2008; Isaksen & Stoffelen, 2000), used operationally for coastal (Lislie et al., 2008; Milliff & Stamus, 2008) and tropical cyclone (Brennan et al., 2008; Singh et al., 2008) wind forecasting, in global scale and mesoscale meteorology studies (Chelton et al., 2004; Liu et al., 1998; Zecchetto & Cappa, 2001), in climatological studies (Kolstad, 2008; Risien & Chelton, 2008; Zecchetto & De Biasio, 2007), in the assessment of the performances of the global (Chelton & Freilich, 2005) and regional atmospheric models (Accadia et al., 2007), in the oceanic simulations (Milliff et al., 2001; Ruti et al., 2008).

2.1.1 SeaWinds on board of QuikSCAT satellite

QuikSCAT is a NASA satellite launched in June 1999. It provides, by means of the on board scatterometer *SeaWinds* working at Ku band (13.4 GHz), wind fields with spatial resolution of 25 km × 25 km and 12.5 km × 12.5 km at neutral air-sea stability conditions. *SeaWinds* is a scatterometer with a rotating antenna, measuring the wind in swaths 1800 km wide. Because of the operating frequency, *QuikSCAT* data can be seriously contaminated by rain (Jones et al., 1999; Portabella & Stoffelen, 2001). For this reason the wind data are provided with the probability that the columnar rate of rain exceeds 2 km mm h⁻¹, (Huddleston & Stiles, 2000), which can be used to discard the contaminated data. Figure 1 reports a *SeaWinds* swath over the European waters.

The data used here are the level L2B data set, available at PODAAC². According to the sensor specifications, the *QuikSCAT* winds have an accuracy of 2 ms⁻¹ in speed and 20° in direction in the wind speed range 3-20 ms⁻¹, but the actual accuracies are generally better (1 m s⁻¹ and 23° (Ebuchi et al., 2002), 1.3 m s⁻¹ and 27° (Pickett et al., 2003), 1.7 m s⁻¹ and 14° (Chelton & Freilich, 2005)).

² available at podaac.jpl.nasa.gov/pub/ocean_wind/quikscat

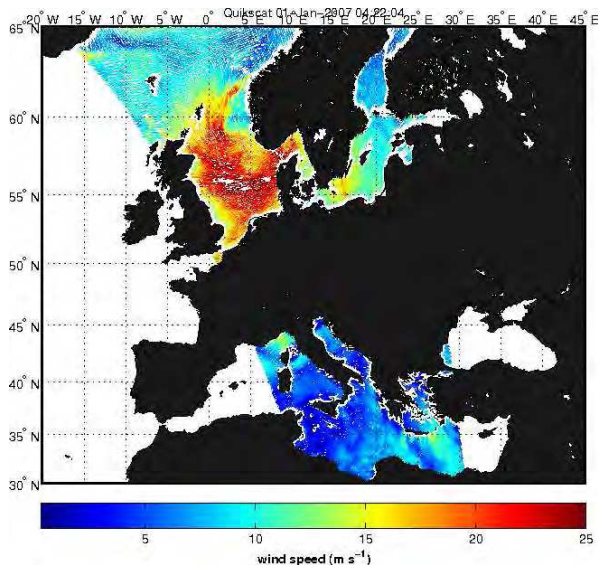


Fig. 1. A swath of *SeaWinds* over the European waters. 1 January 2007 at 04:22 GMT. Ascending orbit.

2.1.2 ASCAT on board of Metop satellite

Since May 2007, the European satellite *Metop* is operational: among other instruments, it carries the scatterometer *ASCAT*. Differently from *QuikSCAT*, *ASCAT* has fixed antennas in the two sides of the satellite, producing a swath composed by two sub-swaths 500 km wide, 768 km apart. The available spatial resolutions are 25 km by 25 km and 12.5 km by 12.5 km. Working at C-band (5.255 GHz), *ASCAT* data are only slightly affected by rain. Figure 2 reports a swath of *ASCAT* over the European waters at spatial resolution of 25 km by 25 km. *ASCAT* wind data are available at Eumetsat³ or in near real time from the Dutch Met Office (www.knmi.nl), disseminating the data on behalf of the Ocean & Sea Ice Satellite Application Facility (www.osi-saf.org) of EUMETSAT (www.eumetsat.org).

2.2 The Synthetic Aperture Radar

At present, several Synthetic Aperture Radar (SAR) instruments are flying above us: the Advanced SAR instrument of *Envisat* (March 2002) (ESA, 2002), the German *TerraSAR-X* (June 2007) (DLR, 2003), the Italian *Cosmo-SkyMed* programme (from June 2007) (ASI, 2007), the Canadian commercial satellite *RADARSAT-2* (December 2007) (CSA, 2001; Morena et al., 2004). Table 1 reports the main characteristics of the mentioned SARs.

The term polarization refers to the polarization of the transmitted Tx and received Rx electromagnetic waves. Single polarization can be (TxRx) VV or HH or VH or HV; dual polarization comprises HH and HV or VV and VH; quad (fully) polarization is when all the possible polarization combinations are acquired, i. e. HH, HV, VV, VH. *Terrasar-X*, *CosmoSkyMed* and *RADARSAT-2* are fully polarimetric SARs.

³ <http://archive.eumetsat.int/umarf/>

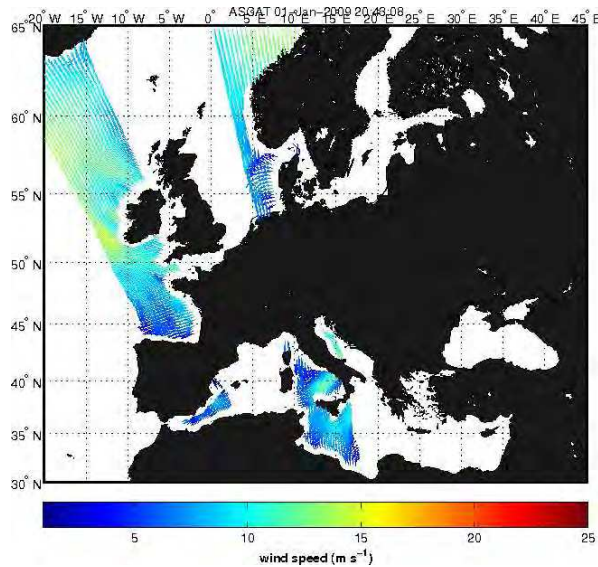


Fig. 2. A swath of ASCAT over the European waters. 1 January 2009 at 20:43 GMT. Ascending orbit.

Satellite	Polarization	Frequency	Spatial resolution (width x length) m	Swath width (km)
Envisat ¹	Single, dual	C-band (5.3 GHz)	Polarization mode: ~ 30 x 30 Wide Swath mode: ~ 150 x 150 Global Monitoring mode: ~ 1000 x 1000	up to 100 400 > 400
TerraSAR-X ²	Single, dual, quad	X-band (9.6 GHz)	SpotLight: up to 1 StripMap: up to 3 ScanSAR: up to 18	10 30 100
Radarsat-2 ³	Single, dual, quad	C-band (5.4 GHz)	Ultra-Fine: 3 x 3 Multi-Look Fine: 8 x 8 Standard: 25 x 26 Wide: 30 x 26 ScanSAR narrow: 50 x 50 ScanSAR wide: 100 x 100 Standard Quad-pol: 12 x 8 Fine Quad-pol: 25 x 8	20 50 100 150 300 500 25 25
CosmoSkyMed ⁴	Single, dual, quad	X-band (9.6 GHz)	Spotlight-2: 1 x 1 Stripmap: 3 x 3 5 x 5 Scansar: 30 x 30 100 x 100	10 30 40 100 200

Table 1. The main characteristics of the operational SAR instruments. From: ¹envisat.esa.int; ²www.infoterra.de/terrasar-x; ³www.radarsat2.info; ⁴www.e-geos.it/docs/asi.pdf

3. Mesoscale wind meteorology from scatterometer data

The mesoscale may be defined, according to Orlanski (1975), as composed by three subranges: the mesoscale γ , from 2 km to 20 km, β , from 20 km to 200 km and α , from 200 km to 2000 km. This range is of uttermost importance, since in this range the wind controls the atmosphere's dynamics. This range is also sensitive to local modulations of the wind field, especially in regions where steep orography surrounds the various basins. Indeed, this is the range where global models have a decreased ability in reproducing the surface wind field. One of the regions where the atmospheric phenomena frequently occur in the mesoscale range is the Mediterranean Basin, which is chosen here as the area of interest.

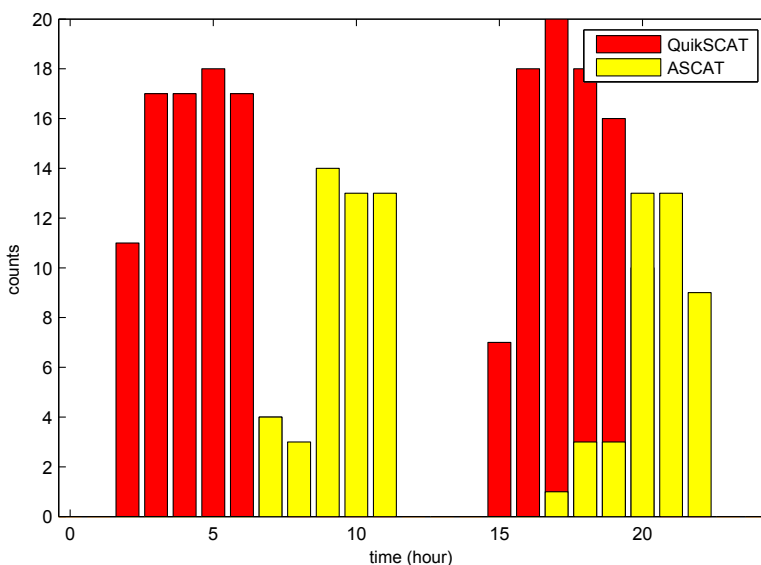


Fig. 3. Frequency distribution of QuikSCAT (red) and ASCAT (yellow) passes over the Mediterranean Basin as a function of the day time (GMT). January 2008.

The Mediterranean Basin is a semi-enclosed basin, having maximum extent of about 4000 km east-west and of about 1200 km north-south. It is almost entirely surrounded by mountain chains (with the exception of the east coast of Tunisia), which often raise nearby the coastline. The complexity of the coastal orography and the presence of mountainous islands deeply influence the local scale atmospheric circulation in the MABL, producing local effects at spatial scales down to a few kilometers. In the Mediterranean Basin, many regional wind systems, local cyclogenesis and wind flow disturbances induced by orography have a spatial variability at the mesoscale β . Up to now, the atmospheric phenomena at this scale in the Mediterranean Basin have not been extensively studied, mainly due to the lack of high spatial resolution data.

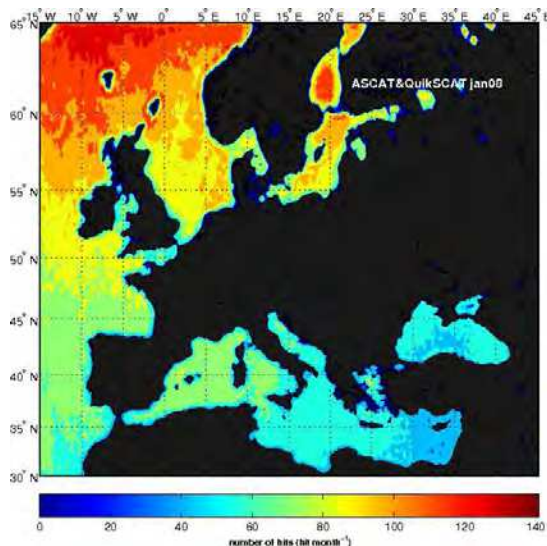


Fig. 4. Monthly coverage of QuikSCAT and ASCAT scatterometers over the European waters. January 2008.

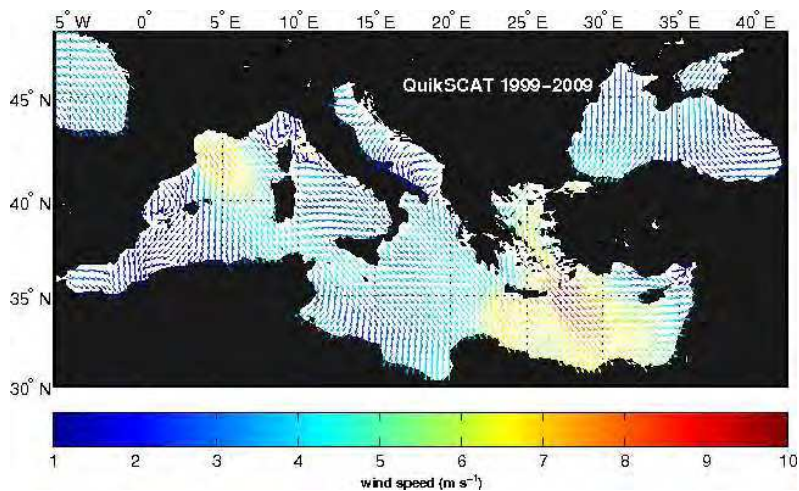


Fig. 5. Mean wind speed field over the Mediterranean Basin (July 1999 to May 2009) derived from QuikSCAT data. The vectors are plotted at one third of their original space resolution for readability

3.1 Parameters describing the wind field characteristics

Besides the mean wind field, several other parameters are important in defining the wind spatial structure, i. e. the wind gustiness, the wind steadiness and the wind speed variability.

The wind speed gustiness G is defined as:

$$G = \left(\sum_{i=1}^n (U_i - \bar{U})^2 \right)^{1/2} / \bar{U} \quad (1)$$

where U_i is the wind speed modulus at time i , and \bar{U} the mean value of ensemble $\{U_i\}$. The gustiness is a non-dimensional parameter providing information on the turbulent intensity of the wind. All the previous quantities are related to wind speed, neglecting wind direction. The wind steadiness coefficient S , expressed as

$$S = 100 \frac{[(\sum_{i=1}^n (u_i)^2) + (\sum_{i=1}^n (v_i)^2)]^{1/2}}{\sum_{i=1}^n (u_i^2 + v_i^2)^{1/2}} \quad (2)$$

where u_i and v_i are the zonal and meridional wind components, provides insights into the variability of the wind direction. This non-dimensional parameter, which expresses the ratio between the mean vector and the mean scalar wind speed, ranges from 0 (wind direction randomly changing) to 100 (constant wind direction). It permits the identification of persistent wind regimes. The wind speed variability σ_w is the wind standard deviation computed over the period considered, and may be considered to integrate the information provided by the non-dimensional gustiness.

3.2 Temporal sampling and spatial coverage

To study the climatological spatial properties of a field, it is important to know how it has been produced and the temporal sampling of the area of interest.

One of the important aspects concerns the scatterometer pass time over a region of interest. Considering the Mediterranean Basin, the pass time of QuikSCAT and ASCAT, regardless the number of data per passage, may be inferred from Fig. 3, which reports the frequency distribution of the pass time as a function of the day time for January 2008. QuikSCAT swaths the Mediterranean Basin in the early morning and early afternoon, while ASCAT in the middle morning and evening. Figure 4 reports the map of the number of hits provided by QuikSCAT and ASCAT together over the European waters for one month (January 2008). The sampling roughly increases with latitude, from the ≈ 50 hit month⁻¹ of the eastern Mediterranean to the ≈ 140 hit month⁻¹ above 60°. In the Mediterranean Basin there are about two measurements per day: this permits to represent the temporal evolution of the wind only at scales longer than one day, but prevents to study of the wind associated to phenomena like fronts or cyclogenesis.

With the present coverage provided jointly by QuikSCAT and ASCAT in the Mediterranean Basin, it is possible to study the spatial structure of the winds in the mesoscale α and β , while their temporal evolution only in the mesoscale α .

3.3 Climatological spatial structure of the wind

The short time climatology of the spatial structure of the wind has been built over the ten years of QuikSCAT data available (July 1999 to May 2009), and presented here in terms of seasonal fields. To illustrate some aspect of the climatological spatial structure of the wind over the Mediterranean Basin, the winter and summer maps of wind speed variability σ_w and of wind steadiness S are presented. Before to present them, it is useful to sketch the general characteristics of the large scale wind circulation over the Mediterranean basin.

The Mediterranean weather is mainly driven by the Atlantic weather which, locally modified over the Mediterranean area (HMSO, 1962), produces a secondary weather system of spatial scales smaller than 500 km or so, frequent in all seasons. This is due both to the basin size and its geographic configuration: the coastal steep orography and the presence of large islands may modify the synoptic scale air flows over the region producing well distinct circulations on regional scale (Zecchetto & Cappa, 2001; Zecchetto & De Biasio, 2007). Many of the most important regional winds in this basin are indeed the product of the interaction between the synoptic scale flow and the local orography. However, the Mediterranean Sea, due to its longitudinal extension, can be subject to various (sometimes co-existing) circulation regimes as, for instance, the etesian wind circulation in the Eastern Mediterranean during summer, mainly linked to the Asian Monsoon (Ziv et al., 2004).

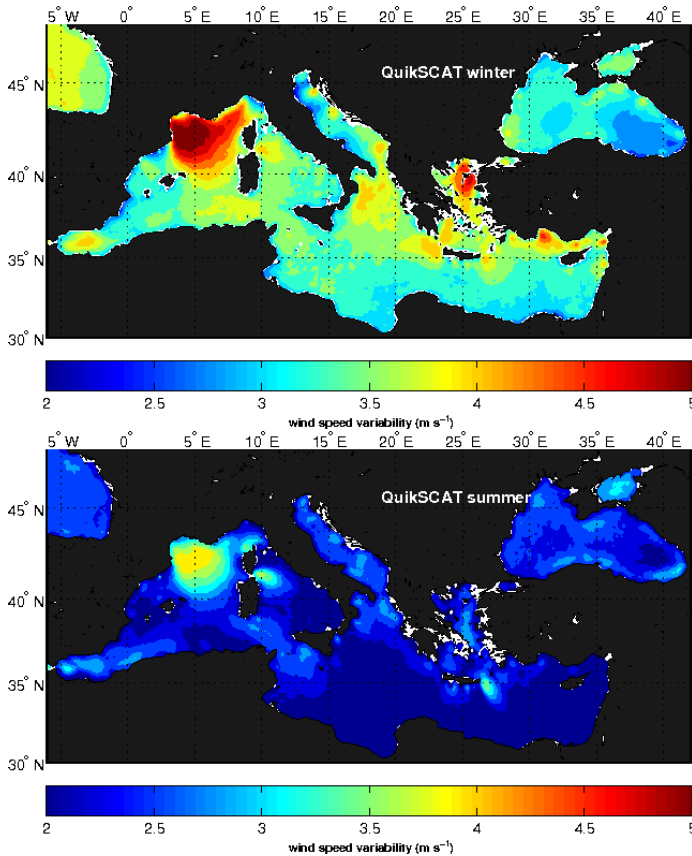


Fig. 6. Seasonal wind speed variability over the Mediterranean Basin (July 1999 to May 2009) derived from QuikSCAT data. Top panel: winter. Bottom panel: summer.

Figure 5 reports the QuikSCAT mean wind field over ten years (July 1999 to May 2009), plotted at one third of its original space resolution for readability. The basin scale wind circulation is mainly from northwest, with a strong signature of mistral in the Gulf of Lion and of the

etesian in the eastern part of the basin. However, several regional wind circulations are co-existing, such as the northeastern bora wind (Pandžić & Likso, 2005; Yoshino, 1976) affecting the Adriatic Sea, and the northern winds of Black Sea, where a cyclonic circulation dominates the eastern part of the basin and an anticyclonic one prevails in its western side (Efimov & Shokurov, 2002).

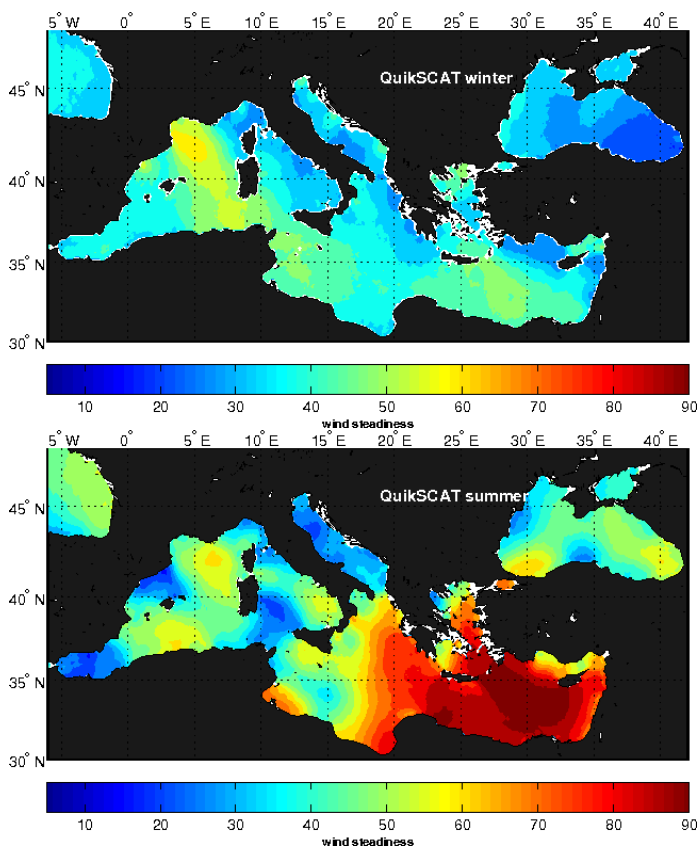


Fig. 7. Seasonal wind steadiness over the Mediterranean Basin (July 1999 to May 2009) derived from QuikSCAT data. Top panel: winter. Bottom panel: summer.

Figure 6 reports the maps of wind speed variability (top panel) for winter (December to February) and summer (June to August, bottom panel). Keeping in mind the general circulation shown in Fig. 5, it is easy to attribute the highest wind variability, found in areas at the wind lee side, to the influence of the interaction between the wind flow and the orography. This is particularly evident between Corsica and Sardinia and between Crete and Rhodos islands in the eastern basin in winter and summer, both due to the funneling and island shielding effects. The orographically induced effects may be seen also in Adriatic and Aegean seas in winter and in the southern Turkey. Figure 7 reports the maps of wind steadiness for winter (top panel) and summer (bottom panel). The highest steadiness is found in the eastern Mediterranean in summer, as effect of the etesian wind circulation. In winter,

the moderate steadiness is highest in the area interested by the mistral (Gulf of Lion up to the Sicily Channel) and south of the Crete-Rhodos islands. In this season, also the steadiness pattern in the Adriatic Sea reveals the signature of the northeastern bora.

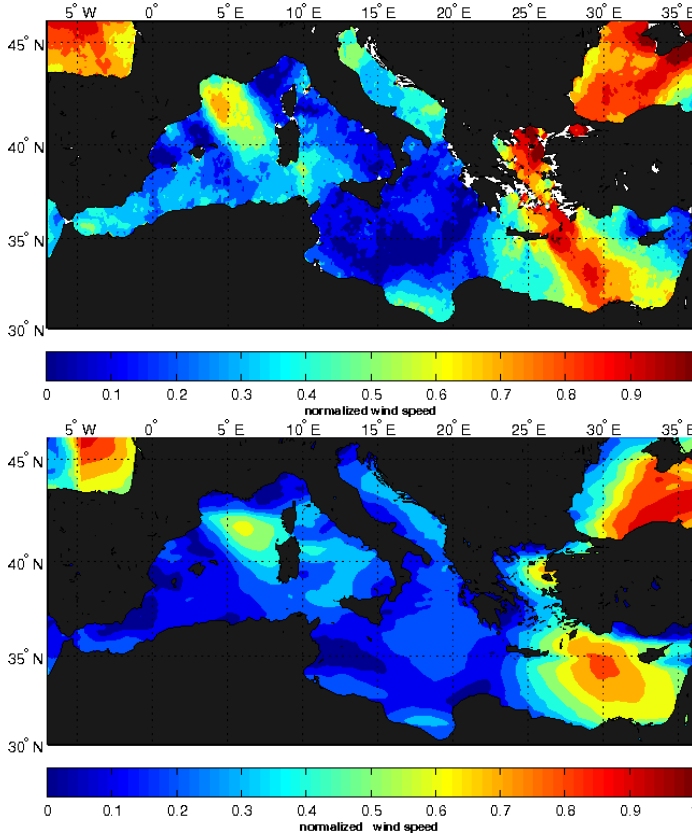


Fig. 8. Normalized mean wind speed fields from QuikSCAT (top panel) and QBOLAM (bottom panel) over the Mediterranean. October 2000.

3.4 Atmospheric models and scatterometer wind fields

This section is aimed to show similarities and differences of the wind fields derived from scatterometer and from a regional atmospheric model, a topic faced in Accadia et al. (2007). The surface wind has been forecasted by a limited area model, the Quadrics Bologna Limited-Area Model (QBOLAM) (Speranza et al., 2004), a parallelized version of BOLAM (Buzzi et al., 1994), covering the whole Mediterranean area with 0.1° by 0.1° grid resolution. Figure 8 reports the fields of the normalized mean wind speed for October 2000, as derived from QuikSCAT (top panel) and QBOLAM (bottom panel). The fields are normalized to make them more comparable. Apart from the differences on the spatial structure of the wind (the model winds are more westerlies than those measured by scatterometer), note the different representation of details provided by the two fields. Despite QBOLAM has a nominal spatial

resolution of 0.1° (about 10 km in latitude and 7 km in longitude), higher than that of scatterometer (12.5 km by 12.5 km), its fields result smoother. This common feature of the model fields, discussed in Chèruy et al. (2004) and Skamarock (2004), stresses the importance of the satellite winds in studying the mesoscale spatial features of the wind.

4. Small-scale structure of the MABL from SAR images

The increased availability of satellite SAR images offers to scientists many opportunities to investigate the structure of the MABL over the sea and coastal areas. Scientific literature about SAR images over the ocean has shown a variety of geophysical phenomena detectable by SAR (Alpers & Brümmer, 1994; Kravtsov et al., 1999; Mitnik et al., 1996; Mityagina et al., 1998; Mourad, 1996; Sikora et al., 1997; Zecchetto et al., 1998), including the multiscale structure in the atmospheric turbulence under high winds and the structure of the convective turbulence under low wind. More recently, some effort has been devoted to evaluate the wind direction, using the backscatter signatures produced by the atmospheric wind rolls or those occurring at the lee side of islands (Vachon & Dobson, 2000) as effect of wind shielding, by computing the local gradient of the image backscatter (Horstmann et al., 2002; Koch, 2004) or by using the two dimensional Continuous Wavelet Transform (CWT2) (Zecchetto & De Biasio, 2002; Zecchetto & De Biasio, 2008).

This section illustrates the ability of the CWT2 in detecting and quantifying the backscatter pattern linked to the spatial structure of the MABL. It summarizes the CWT2 methodology applied to SAR images, providing the results obtainable by showing a case study chosen among the hundreds of images analyzed. The extraction of the wind field from SAR images, a follow up of the CWT2 analysis, is then illustrated at the end.

4.1 The methodology

The Continuous Wavelet Transform (Beylkin et al., 1992; Fofoula-Georgiou & Kumar, 1994) \tilde{f} of a function $f(u)$ is a local transform, dependent on the parameters s and τ , defined as

$$\tilde{f}(s, \tau) = \langle \psi_{(s,\tau)}, f \rangle = \int_{-\infty}^{+\infty} du \psi_{(s,\tau)}^*(u) f(u) \quad (3)$$

where $\psi_{(s,\tau)}(u) = \psi\left(\frac{u-\tau}{s}\right)$ is the mother wavelet at a given scale (or dilation) s and location τ (the asterisk denotes complex conjugation). The quantity $|\tilde{f}(s, \tau)|^2$ plays the role of local energy density at given (s, τ) . The Continuous Wavelet Transform in two dimensions (CWT2) is then,

$$\tilde{f}(s_x, \tau_x; s_y, \tau_y) = \iint_{-\infty}^{+\infty} du dv \psi_{(s_x, \tau_x)}^*(u) \psi_{(s_y, \tau_y)}^*(v) f(u, v).$$

The CWT2 has been computed using the Mexican Hat as mother wavelet, able to capture the fine scale structure of the data and suitable for the continuous wavelet transform because it is non-orthogonal.

The images must be preprocessed before the CWT2 analysis, to mask the land and to mitigate the effects introduced by the variation in range of the radar incidence angle. This avoids that structures on the inner part of the image, where the radar incidence angle is smaller and the radar backscatter higher, prevail on the outer ones.

The choice of the scales is very important because it defines the geophysical phenomena to investigate: if the wind field retrieval is of interest, the spatial range is set from 300 m to 4 km; if phenomena such as the atmospheric gravity waves are the object of study, the spatial range has to be set from 4 km up to 20 km.

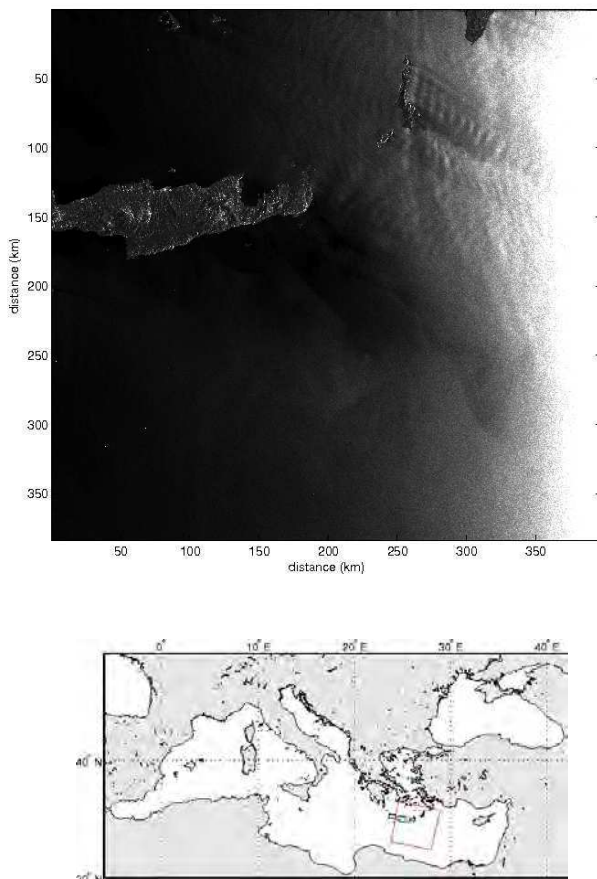


Fig. 9. The Envisat ASAR Wide Swath image selected for the case study. Top panel: the ASAR image (15-May-2008 at 08:20:47 GMT). Bottom panel: the image location in the Mediterranean Sea.

A basic quantity yielded by the CWT2 is the wavelet variance map, derived from the wavelet coefficients. Providing information about the energy distribution as a function of (s_r, s_c) , in the same way as the two dimensional Fourier spectrum does as a function of wavenumbers, it is used to select the scales, taken around the maximum of the wavelet variance map, to build a SAR-like map (reconstructed map). This is obtained adding the wavelet coefficient maps at the selected scales: a SAR-like image is thus obtained, representing a spatial pattern due to the most energetic spatial scales present in the original SAR image.

The reconstructed map undergoes a threshold process to isolate the structures from the background. The result of this procedure is a map of backscatter cells, then used as a mask on the original SAR image to get the values of the radar backscatter inside the detected cells, as well as to estimate their shape and size. The reconstructed map depends on the range of

scales chosen in the analysis. As used here, the CWT2 methodology acts as a filtering based on energetic considerations.

4.2 A case study

The image selected for the case study (Fig. 9, top panel) is an Envisat ASAR Wide Swath image taken in the Crete island area (eastern Mediterranean Sea, Fig. 9, bottom panel). This image covers about 400 km by 400 km, with a pixel resolution of 75 m by 75 m. It has been downloaded from the ESA site⁴.

The tilting effect due to the change of the radar incidence angle - from 16° on the right side to 43° on the left side, hinders to see the fine structure of the radar backscatter, however well visible in the image blow-up reported in Fig. 10: the wind rolls may be seen in many parts of this image, especially in its top right part.

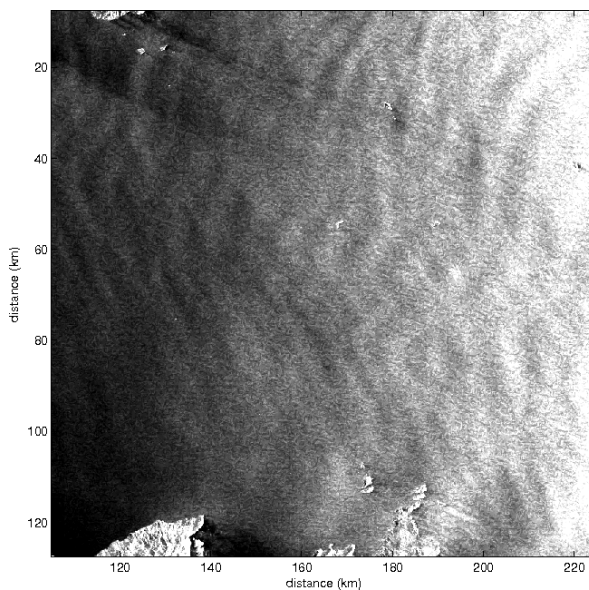


Fig. 10. A blow-up of the ASAR Wide Swath image shown in Fig. 9, roughly corresponding to the area at north-east of Crete.

The larger backscatter structures, as those due to the atmospheric gravity waves east of Karpathos and to the wind sheltering by islands, at the islands lee side (the wind blown from northwest) are easily detectable.

⁴ <http://oa-ip.eo.esa.int/ra/asa>

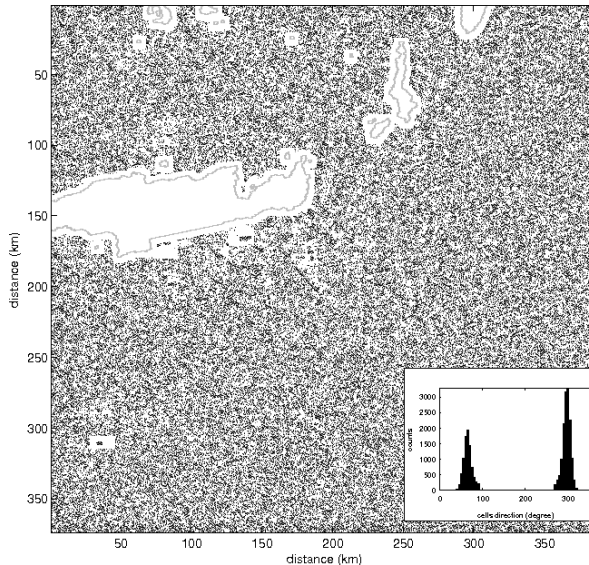


Fig. 11. Map reconstruction in the spatial range $0.3 \text{ km} \div 4 \text{ km}$. Inside panel: the distribution of the orientation of cells' major axis as a function of the angle RGN.

The map reconstructed in the range $0.3 \text{ km} \div 4 \text{ km}$, shown in the left panel of Fig. 11, evidences the small scale structure of the radar backscatter, formed by elliptic cells with major axis orientation falling into two classes, as evidenced by their distribution reported in the inset. The existence of these two classes is due to the texture of the SAR images, and does not represent the geophysical pattern of the backscatter cells excited by the turbulent wind, which may be singled out taking those with directions close to the most probable one, in this case $\theta = 300^\circ$. Thus a reconstructed map with only the cells produced by the wind can be obtained. Figure 12 reports it for the whole image of Fig. 9 (left panel) and for a portion of it (right panel). Note the uneven spatial distribution of the cells but also the high spatial resolution of information obtained. From this map, used as a mask over the original one, it is then possible to retrieve the wind field (Zecchetto & De Biasio, 2008) and to produce a statistics of the cell's size, which may have important implications of the study of the air-sea interaction because it can be linked to the structure of the MABL.

The map reconstructed in the range $4 \text{ km} \div 20 \text{ km}$, reported in the left panel of Fig. 13, clearly shows the pattern of the atmospheric gravity waves in its upper right part. The two dimensional spectral analysis of this map yields the 2D spectrum shown in the right panel of Fig. 13, where two directions are evidenced: that of the maximum energy, occurring at a peak wavelength of 8350 m and an aliased direction of propagation of 296° , and a secondary one, due to the presence of different atmospheric gravity wave trains in the image, with a peak wavelength of 16.7 km and a direction of 63° .

These information may be used, as in Sikora et al. (1997), to estimate the vertical thickness of the MABL.

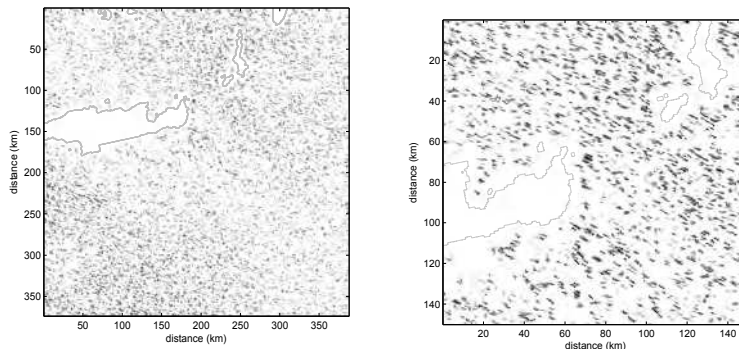


Fig. 12. Reconstructed map with only the cells produced by the wind. Left panel: whole map, corresponding to Fig. 9. Right panel: a blow up of it.

4.3 Wind field extraction: choice of the wind aliased direction

The aliased wind orientation is taken as that corresponding to the most frequent mode of the distribution of cell's direction: in the example reported, the directions around $\Phi = 300^\circ$ have a frequency of 54%, whereas those around $\Phi = 60^\circ$ a frequency of 46%. These frequencies may differ more in some case (70% to 30% or so), while in some other they can result very similar making difficult the choice of the aliased direction. Their variability across the SAR data set likely depends on the characteristics of the images.

4.4 Wind field extraction: dealiasing

The dealiasing technique takes advantage of the idea, formulated by Zecchetto et al. (1998) in a case of convective turbulence, that the wind gustiness, modulating the mean wind speed, produces patches of roughness characterized by an asymmetric distribution of energy along the wind direction. The speed modulation acts inside the cells: higher backscatter is expected at the leading edge of the patches, then decreasing towards the trailing edge, allowing the wind direction dealiasing. This figure is coherent with the layout of the wind cells, organized like "pearls on a string" (Etling & Brown, 1993), as well as with their inner structure (Zecchetto & De Biasio, 2002).

4.5 Wind field extraction: wind speed computation

Once assessed the wind direction, the speed has been computed from the mean radar backscatter of the selected cells using the CMOD5 model (Hersbach et al., 2007), an empirical model converting the radar cross section at C-band to the wind speed, once the radar incidence angle and the wind direction are known.

4.6 The resulting wind field

The wind field derived from the ASAR image of Fig. 9 is shown in the left panel of Fig. 14, along with the contour plot of the wind speed in the right panel. The wind field is spatially uneven because it has been computed over the detected cells. Where the wind is low, as at

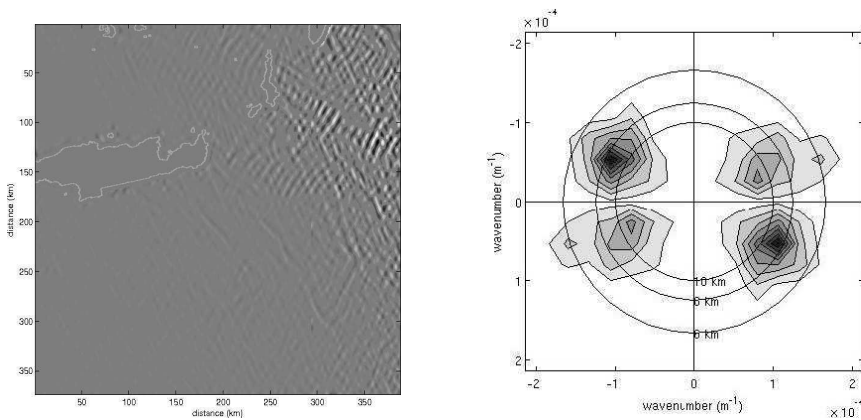


Fig. 13. Map reconstruction in the spatial range $4 \text{ km} \div 20 \text{ km}$. Left panel: the reconstructed map. Right panel: the 2D power spectrum of the reconstructed map.

the lee side of eastern Crete, the spatial density of cells is low too and the wind vectors result more sparse.

The SAR derived wind field provides very detailed information about the spatial structure of the wind and an estimate of the wind much closer to coast than scatterometer, as the Fig. 15, which reports the QuikSCAT wind field at 12.5 km of resolution (left panel) and the contour plot of the wind speed (right panel) suggests.

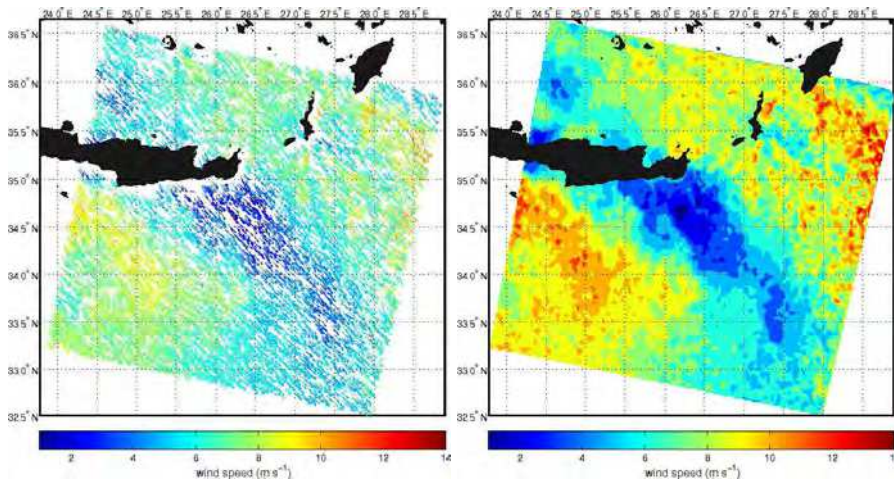


Fig. 14. The wind field derived from the processing with CWT2 method of the ASAR image of Fig. 9. Left panel: the wind field. Right panel: contour map of the wind speed.

Thus, SAR derived winds are an unique experimental tool for coastal wind study in the mesoscale β and γ .

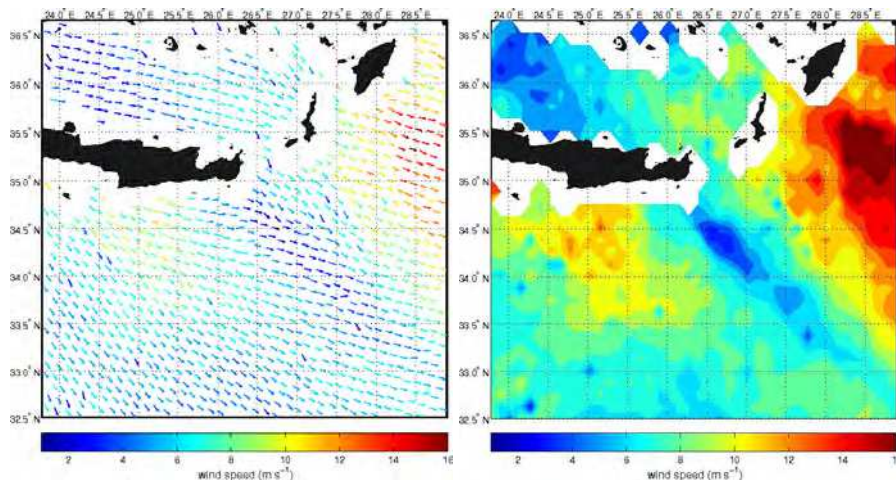


Fig. 15. The wind field from QuikSCAT in the area imaged by ASAR, taken 8 hours and 57 minutes later the ASAR pass time. Left panel: the wind field. Right panel: contour map of the wind speed.

5. Conclusions

This chapter has introduced the satellite scatterometer and SAR, the two satellite radar sensors which may be used to evaluate the wind fields over the sea. A third instrument, the radar altimeter, able to provide only the wind speed over the satellite track, has not been treated because it hardly can be used for mesoscale wind study.

Scatterometer is the most experienced sensor for the measure of the wind field, and its ability to detect detailed features of the wind in the mesoscale is well known. The spatial resolution it provides is sufficient for open sea applications, but insufficient for coastal wind studies, since the data closest to coast are at least 25 km away. Furthermore, the temporal sampling at middle latitudes, roughly two samples per day, is still insufficient for a suitable description of the time evolution of the winds associated to the frontal passage or local cyclogenesis.

The SAR derived wind fields solve the problem of coverage close to coasts, providing very resolute wind fields and permitting to infer the wind speed variability in these areas, as done by Young et al. (2008). Concerning the time sampling provided by operative SARs, this is an open question, the answer depending on many factors: the imaging capabilities of satellites (Radarsat2 has an imaging capability of 28 minutes/orbit, Envisat ASAR 30 minute/orbit for imaging modes and all orbit in the Global Monitoring Mode), the priorities of the different SAR missions (SAR is used over land and over sea), the spatial resolution required. To provide some number, the Envisat ASAR has an average revisit of seven days at the equator, improving to nearly every five days at 45°. With such a revisit time, only research applications can be envisaged, as a monitoring of whatever atmospheric phenomenon would suffer for the unsuitable time sampling. However, the constellations of satellites like the CosmoSkyMed mission, will offer, in principle, a revisiting period of < 12 hours, approaching the threshold of six hours considered the minimum time sampling to describe the evolution of the winds.

Acknowledgments

Scatterometer QuikSCAT data have been downloaded from the Physical Oceanography Distributed Active Archive Center (PODAAC) of the Jet Propulsion Laboratory, Pasadena, USA. The ASCAT data have been obtained from the Koninklijk Nederlands Meteorologisch Instituut (Dutch Meteorological Service KNMI, www.knmi.nl) operating in the framework of the Ocean & Sea Ice Satellite Application Facility (www.osi-saf.org) of EUMETSAT. The Envisat ASAR Wide Swath image has been downloaded from the ESA web server <http://oa-ip.eo.esa.int/ra/asa> on the framework of the Project Start Up C1P.5404 of the European Space Agency.

6. References

- Accadia, C., Zecchetto, S., Lavagnini, A. & Speranza, A. (2007). Comparison of 10-m wind forecasts from a regional area model and QuikSCAT scatterometer wind observations over the Mediterranean Sea, *Monthly Weather Review* **135**: 1946–1960.
- Alpers, W. & Brümmer, B. (1994). Atmospheric boundary layer rolls observed by the synthetic aperture radar aboard the ERS-1 satellite, *Journal of Geophysical Research* **99**(C6): 12613 – 12621.
- ASI (2007). COSMO-SkyMed system description and user guide, *Technical Report ASI-CSM-ENG-RS-093-A*, Agenzia Spaziale Italiana, Rome, Italy.
- Beylkin, G., Coifman, R., Daubechies, I., Mallat, S., Meyer, Y. & Raphael, L. (1992). *Wavelets and their applications*, Jones and Barlett Publishers, Boston.
- Brennan, M. J., Hennon, C. C. & Knabb, R. D. (2008). The operational use of QuikSCAT ocean surface vector winds at the National Hurricane Center, *Weather and Forecasting* **23**: 168182. (doi: 10.1175/2008WAF2222188.1).
- Buzzi, A., Fantini, M., Malguzzi, P. & Nerozzi, F. (1994). Validation of a limited area model in cases of Mediterranean cyclogenesis: Surface fields and precipitation scores, *Meteor. Atmos. Phys.* **53**: 53–67.
- Campbell, A. B. (2002). *Radar remote sensing of planetary surfaces*, Cambridge University Press, Cambridge.
- CCRS (2009). Tutorial: Fundamentals of Remote Sensing, *Technical report*, Canada Centre for Remote Sensing, <http://www.ccrs.nrcan.gc.ca/resource/tutor/gsarcd>.
- Chelton, D. & Freilich, M. (2005). Scatterometer-based assessment of 10-m wind analyses from the operational ECMWF and NCEP numerical weather prediction models, *J. of Geophys. Res.* **133**: 409–429.
- Chelton, D., Schlax, M. G., Freilich, M. & Millif, R. F. (2004). Satellite radar measurements reveal short-scale features in the wind stress field over the world ocean, *Science* **303**: 978–983.
- Chèruy, F., Speranza, A., Sutera, A. & Tartaglione, N. (2004). Surface winds in the Euro-Mediterranean area: the real resolution of numerical grids, *Annales Geophysicae* **22**: 4043–4048.
- CSA (2001). Applications potential of RADARSAT-2 - A Preview, *Technical report*, Canadian Space Agency. (J. J. Van der Sanden and S. G. Ross eds.).
- DLR (2003). TerraSAR-X Science Plan, *Technical Report TX-PGS-PL-4001*, Deutschen Zentrums für Luft- und Raumfahrt (DLR), Oberpfaffenhofen, Germany.

- Ebuchi, N., Graber, H. & Caruso, M. J. (2002). Evaluation of wind vectors observed by QuikSCAT/SeaWinds using ocean buoy data, *J. of Atmosph. and Oceanic Tech.* **19**: 2049–2062.
- Efimov, V. V. & Shokurov, M. V. (2002). Spatiotemporal structure of the surface wind field over the Black Sea, *Izvestiya Atmospheric and Oceanic Physics* **38**(4): 421–430.
- Elachi, C. (1988). *Spaceborne Radar Remote Sensing: Applications and Techniques*, IEEE Press, New York, USA.
- ESA (2002). ASAR Product Handbook, *Technical report*, European Space Agency, Paris, France.
- Etling, D. & Brown, R. A. (1993). Roll vortices in the planetary boundary layer: a review, *Boundary Layer Meteorol.* **65**: 15–248.
- Eumetsat (2007). ASCAT Wind Product User Manual, *Technical Report SAF/OSI/CDOP/KNMI/TEC/MA/126*, Eumetsat, Darmstadt, Germany.
- Foufoula-Georgiou, E. & Kumar, P. (eds) (1994). *Wavelet in Geophysics*, Vol. 4 of *Wavelet analysis and its applications*, Academic Press, San Diego, CA.
- Hersbach, H., Stoffelen, A. & de Haan, S. (2007). An improved scatterometer ocean geophysical model function: CMOD5, *Journal of Geophysical Research* **112**: 5767–5780. doi:10.1029/2006jc003743.
- HMSO (1962). *Weather in the Mediterranean, Volume 1 (second ed.)*, Her Majesty's Stationary Office, London, UK.
- Horstmann, J., Koch, W. & Lehner, S. (2002). High resolution wind fields retrieved from SAR in comparison to numerical models, *Proceedings of the IEEE International Geoscience and Remote Sensing Symposium*, Toronto, Canada.
- Huddleston, J. M. & Stiles, B. W. (2000). Multidimensional histogram (mudh) rain flag. Product description ver. 2.1, *Technical report*, Jet Propulsion Laboratory, Pasadena, USA.
- Isaksen, L. & Janssen, P. A. E. M. (2008). Impact of ERS scatterometer winds in ECMWF's assimilation, *Q. J. R. Meteorol. Soc.* **130**: 1793–1814.
- Isaksen, L. & Stoffelen, A. (2000). ERS scatterometer wind data impact on ECMWF's tropical cyclone forecasts, *IEEE Trans. Geosci. Remote Sens.* **138**: 1885–1892.
- Jones, W. L., Mladen, S., Park, J. & Mehershadi, R. (1999). A quality control rain flag using QuikSCAT radiometric observations, *Proc. of QuikSCAT Cal / Val Workshop*, Pasadena, USA.
- JPL (2006). QuikSCAT Science Data Product User's Manual (Ver. 3), *Technical Report Publ. D-18053*, Jet Propulsion Laboratory, Pasadena, USA.
- Koch, W. (2004). Directional analysis of SAR images aiming at wind direction, *IEEE Trans. Geosci. Remote Sens.* **42**(4): 702 – 710.
- Kolstad, E. W. (2008). A QuikSCAT climatology of ocean surface winds in the nordic seas: identification of features and comparison with the NCEP/NCAR reanalysis, *Journal of Geophysical Research* **113**. D11106, doi:10.1029/2007JD008918.
- Kravtsov, Y., Mityagina, M., Pungin, V. & Sabinin, K. (1999). Manifestation of the wind-field fine structure ahead of an atmospheric cold front on radar imagery of the sea surface, *Earth Obs. Rem. Sens.* **5**: 513–525.
- Lislie, L. M., Buckley, B. W. & Lepastier, M. (2008). The operational impact of QuikSCAT winds in Perth, Australia: examples and limitations, *Weather and Forecasting* **23**(1): 183–193. (doi: 10.1175/2007WAF2007027.1).

- Liu, T. W., Tang, W. & Polito, P. S. (1998). NASA scatterometer provides global ocean-surface wind fields with more structures than numerical weather prediction, *Geophysical Research Letters* **25**: 761–764.
- Milliff, R. F., Morzel, J., Danabasoglu, G. & Chin, T. M. (2001). Ocean general circulation model sensitivity to forcing from scatterometer winds, *J. Geophys. Res.* **104C**: 11337–11358.
- Milliff, R. F. & Stamus, P. A. (2008). QuikSCAT impacts on coastal forecasts and warnings: operational utility of satellite ocean surface vector wind data, *Weather and Forecasting* **23**(5): 878890. (doi: 10.1175/2008WAF2007081.1).
- Mitnik, L., Hsu, M. & Mitnik, M. (1996). Sharp gradients and organised structures in sea surface wind field in the region of polar vortex formation, *Global Atmos. Ocean Syst.* **4**: 335–361.
- Mityagina, M., Pungin, V. & Yakovlev, V. (1998). Two-polarization K_u -band radar imagery of the sea surface in presence of atmospheric boundary layer motions, *Waves Random Media* **8**: 111–118.
- Monahan, E. C. (2002). The physical and practical implications of CO_2 gas transfer coefficient that varies as the cube of the wind speed, in E. S. S. M. A. Donelan, W. M. Drennan & R. Wanninkhof (eds), *Gas transfer at water surface*, American Geophysical Union, Washington DC, USA, pp. 193–197.
- Morena, L. C., James, K. V. & Beck, J. (2004). An introduction to the RADARSAT-2 mission, *Canadian J. Remote Sensing* **30**(3): 221–234.
- Mourad, P. (1996). Inferring multiscale structure in the atmospheric turbulence using satellite-based synthetic aperture radar imagery, *J. Geophys. Res.* **101**: 18433–18449.
- Orlanski, I. (1975). A rational subdivision of scales for atmospheric processes, *Bull. Amer. Meteor. Soc.* **56**: 527–530.
- Pandžić, K. & Likso, T. (2005). Eastern Adriatic typical wind field patterns and large-scale atmospheric conditions, *Int. J. of Climatology* **25**: 81–98.
- Pickett, M. H., Tang, W., Rosenfeld, L. K. & Wash, C. H. (2003). QuikSCAT satellite comparisons with nearshore buoy wind data off the U.S. west coast, *J. of Atmos. and Ocean. Tech.* **20**: 1869–1879.
- Portabella, M. & Stoffelen, A. (2001). Rain detection and quality control of SeaWinds, *J. of Atmos. and Ocean. Tech.* **18**: 1171–1183.
- Risien, C. M. & Chelton, D. B. (2008). A global climatology of surface wind and wind stress fields from eight years of QuikSCAT scatterometer data, *Journal of Phys. Ocean.* **38**(11): 2379–2413. (doi: 10.1175/2008JPO3881.1).
- Ruti, P. M., Marullo, S., D’Ortenzio, F. & Tremant, M. (2008). Comparison of analyzed and measured wind speeds in the perspective of oceanic simulation over the Mediterranean basin: analysed, QuikSCAT and buoy data, *J. of Marine Systems* **70**: 33–48. (doi: 10.1016/j.jmarsys.2007.02.026).
- Sikora, T., Young, G., Shirer, H. & Chapman, R. (1997). Estimating convective atmospheric boundary layer depth from microwave radar imagery of the sea surface, *J. Appl. Meteorol.* **36**: 833–845.
- Singh, R., Pal, P. K., Kishtawal, C. M. & Joshi, P. C. (2008). The impact of variational assimilation of SSM/I and QuikSCAT satellite observations on the numerical simulation of Indian ocean tropical cyclones, *Weather and Forecasting* **23**: 460–476. (doi: 10.1175/2007WAF2007014.1).
- Skamarock, W. C. (2004). Evaluating mesoscale NWP models using kinetic energy spectra, *Monthly Weather Review* **132**: 3019–3032.

- Speranza, A., Accadia, C., Casaioli, M., Mariani, S., Monacelli, G., Inghilesi, R., Tartaglione, N., Ruti, P. M., Carillo, A., Bargagli, A., Pisacane, G., Valentinotti, F. & Lavagnini, A. (2004). POSEIDON: an integrated system for analysis and forecast of hydrological, meteorological and surface marine fields in the Mediterranean area, *Il Nuovo Cimento* **27C**: 329–345.
- Vachon, P. & Dobson, F. (2000). Wind retrieval from Radarsat SAR images: selection of a suitable C-Band HH polarization wind retrieval model, *Canadian Journal of Remote Sensing* **24**(4): 306 – 313.
- Valenzuela, G. (1978). Theories for the interaction of electromagnetic and oceanic waves- A review, *Boundary Layer Meteorology* **13**: 61–85.
- Yoshino, M. (1976). *Local wind Bora*, University of Tokio Press, Tokio, Japan.
- Young, G., Sikora, T. & Winstead, N. (2008). Mesoscale near-surface wind speed variability mapping with synthetic aperture radar, *Sensors* **8**(11): 7012–7034. (doi: 10.3390/s8117012).
- Zecchetto, S. & Cappa, C. (2001). The spatial structure of the Mediterranean Sea winds revealed by ERS-1 scatterometer, *Int. J. Remote Sensing* **22**(1): 45–70.
- Zecchetto, S. & De Biasio, F. (2002). On shape, orientation and structure of atmospheric cells inside wind rolls in SAR images, *IEEE Trans. of Geoscience and Remote Sensing* **40**(10): 2257 – 2262.
- Zecchetto, S. & De Biasio, F. (2007). Sea surface winds over the Mediterranean Basin from satellite data (2000-04): meso- and local-scale features on annual and seasonal time scales, *J. Applied Meteor. and Climatology* **46**: 814–827.
- Zecchetto, S. & De Biasio, F. (2008). A wavelet based technique for sea wind extraction from SAR images, *IEEE Trans. of Geoscience and Remote Sensing* **46**(10): 2983–2989. (doi:10.1109/TGRS.2008.920967).
- Zecchetto, S., Trivero, P., Fiscella, B. & Pavese, P. (1998). Wind stress structure in the unstable marine surface layer detected by SAR, *Boundary Layer Meteorol.* **86**: 1–28.
- Ziv, B., Saaroni, H. & Alpert, P. (2004). The factors governing the summer regime of the eastern Mediterranean, *Int. J. of Climatology* **24**: 1859–1971.



Geoscience and Remote Sensing New Achievements

Edited by Pasquale Imperatore and Daniele Riccio

ISBN 978-953-7619-97-8

Hard cover, 508 pages

Publisher InTech

Published online 01, February, 2010

Published in print edition February, 2010

Our planet is nowadays continuously monitored by powerful remote sensors operating in wide portions of the electromagnetic spectrum. Our capability of acquiring detailed information on the environment has been revolutionized by revealing its inner structure, morphology and dynamical changes. The way we now observe and study the evolution of the Earth's status has even radically influenced our perception and conception of the world we live in. The aim of this book is to bring together contributions from experts to present new research results and prospects of the future developments in the area of geosciences and remote sensing; emerging research directions are discussed. The volume consists of twenty-six chapters, encompassing both theoretical aspects and application-oriented studies. An unfolding perspective on various current trends in this extremely rich area is offered. The book chapters can be categorized along different perspectives, among others, use of active or passive sensors, employed technologies and configurations, considered scenario on the Earth, scientific research area involved in the studies.

How to reference

In order to correctly reference this scholarly work, feel free to copy and paste the following:

S. Zecchetto (2010). Ocean Wind Fields from Satellite Active Microwave Sensors, Geoscience and Remote Sensing New Achievements, Pasquale Imperatore and Daniele Riccio (Ed.), ISBN: 978-953-7619-97-8, InTech, Available from: <http://www.intechopen.com/books/geoscience-and-remote-sensing-new-achievements/ocean-wind-fields-from-satellite-active-microwave-sensors>

INTECH

open science | open minds

InTech Europe

University Campus STeP Ri
Slavka Krautzeka 83/A
51000 Rijeka, Croatia
Phone: +385 (51) 770 447
Fax: +385 (51) 686 166
www.intechopen.com

InTech China

Unit 405, Office Block, Hotel Equatorial Shanghai
No.65, Yan An Road (West), Shanghai, 200040, China
中国上海市延安西路65号上海国际贵都大饭店办公楼405单元
Phone: +86-21-62489820
Fax: +86-21-62489821

© 2010 The Author(s). Licensee IntechOpen. This chapter is distributed under the terms of the [Creative Commons Attribution-NonCommercial-ShareAlike-3.0 License](#), which permits use, distribution and reproduction for non-commercial purposes, provided the original is properly cited and derivative works building on this content are distributed under the same license.